ARTICLES
https://doi.org/10.1038/s41567-020-01144-5

nature physics

Probing bulk topological invariants using leaky photonic lattices

Daniel Leykam[1,2,5] ✉ and Daria A. Smirnova[3,4]

Topological invariants characterizing filled Bloch bands underpin electronic topological insulators and analogous artificial lattices for Bose–Einstein condensates, photonics and acoustic waves. In bosonic systems, there is no Fermi exclusion principle to enforce uniform band filling, which makes measuring their bulk topological invariants challenging. Here we show how to achieve the controllable filling of bosonic bands using leaky photonic lattices. Leaky photonic lattices host transitions between bound and radiative modes at a critical energy, which plays a role analogous to the electronic Fermi level. Tuning this effective Fermi level into a bandgap results in the disorder-robust dynamical quantization of bulk topological invariants such as the Chern number. Our findings establish leaky lattices as a highly flexible platform for exploring topological and non-Hermitian wave physics.

Characterization of topological phases has attracted broad interest throughout the field of physics since the discovery of topological insulators described by the quantized topological invariants of filled electronic bands[1]. Demonstrations of topological phases have spread from electronic condensed matter to bosonic systems such as photonics[2], Bose–Einstein condensates[3] and acoustics[4], where there is no Fermi exclusion principle and hence no concept of band filling. The lack of band filling complicates the measurement of bulk topological invariants, demanding indirect approaches based on observing their protected edge states[5,6], or time-consuming methods based on Bloch band tomography or adiabatic transport[7–10]. Here we propose a platform that overcomes these challenges, enabling the controlled 'filling' of bosonic Bloch bands, direct bulk measurements of their topological invariants and novel analogies between electronic condensed matter and classical wave systems.

We consider wave propagation in shallow lattices supporting a mixture of bound and leaky modes[11–16]. Leaky modes, also known as quasi-normal modes, emerge when the effective coupling strength between the different lattice sites exceeds the potential depth of the site, resulting in modal-energy-dependent radiative losses. While quasi-normal modes have been extensively employed in the modelling of open scattering systems[17], their dynamical properties have received comparatively little attention, particularly in the context of topological phases.

The cutoff energy between the bound and leaky quasi-normal modes is analogous to the electronic Fermi level; all the modes above this energy dynamically decay, analogous to evaporative cooling. By controlling the cutoff energy, one can achieve the controlled filling of a desired number of bands, as illustrated by the schematic in Fig. 1. In effect, an arbitrary initial field profile is projected onto the bound bands; we show that this enables the direct measurement of bulk topological invariants such as the Zak phase and Chern number[18–21]. Additionally, this class of shallow lattices provides a novel platform for exploring non-Hermitian tight-binding models and topological phases with energy-dependent losses[22–31]. We explain and validate our proposal using coupled-mode theory for the Su–Schrieffer–Heeger (SSH) and Haldane models and full-wave simulations of leaky optical waveguide arrays.

Wave propagation in leaky lattices

Many open linear wave systems can be described by the Schrödinger equation:

$$i\partial_t\psi(\mathbf{r},t) = \left[-\frac{1}{2m_{\mathrm{eff}}}\nabla^2 + V(\mathbf{r})\right]\psi(\mathbf{r},t), \qquad (1)$$

where t is the evolution time, m_{eff} is the effective mass of the wave and $V(\mathbf{r})$ is a localized potential profile. For example, equation (1) is equivalent to the paraxial equation for light under the replacements $t \to z$, $\mathbf{r} = (x, y)$, $m_{\mathrm{eff}} \to k_0$ and $V(\mathbf{r}) \to -k_0\delta n(\mathbf{r})/n_0$, where z is the propagation distance, (x, y) are the transverse coordinates, $k_0 = 2\pi n_0/\lambda$ is the wavenumber, n_0 is the ambient refractive index, λ is the free space wavelength and $\delta n(x)$ is the deviation of the refractive index from n_0.

When $V(\mathbf{r})$ describes a lattice of weakly coupled potential wells, the modes shown in equation (1) can be well approximated as eigenvectors of a tight-binding Hamiltonian[2,3]

$$\hat{H} = \sum\nolimits_{m,m'} \hat{a}_m^\dagger H_{mm'} \hat{a}_{m'}, \quad \hat{H}|\phi\rangle = (E + i\gamma)|\phi\rangle, \qquad (2)$$

where $\hat{a}_m^\dagger(\hat{a}_{m'})$ is the creation (annihilation) operator for the field at the mth (m'th) lattice site, the bra–ket notation $|\phi\rangle = (\phi_1, \phi_2, \ldots)^T$ denotes the wave field on a discrete lattice, and E and γ are the real and imaginary parts of the modal eigenvalue, respectively. The diagonal elements of $\hat{H}$ describe the energies of the individual sites, while the off-diagonal terms describe the coupling between them. In the absence of gain or loss, $\hat{H}$ is Hermitian with purely real eigenvalues, $\gamma = 0$. One can make $\hat{H}$ non-Hermitian by introducing gain or loss, for example, via absorption or modal-symmetry-dependent radiative losses[29,30].

Applying a uniform shift to the energies of $\hat{H}$ (that is, $\hat{H} \to \hat{H} - V_0\hat{1}$) does not affect the dynamics, only introducing an irrelevant phase shift. This is because the usual tight-binding

[1]Center for Theoretical Physics of Complex Systems, Institute for Basic Science, Daejeon, Korea. [2]Basic Science Program, Korea University of Science and Technology, Daejeon, Korea. [3]Nonlinear Physics Centre, Australian National University, Canberra, Australian Capital Territory, Australia. [4]Institute of Applied Physics, Russian Academy of Sciences, Nizhny Novgorod, Russia. [5]Present address: Centre for Quantum Technologies, National University of Singapore, Singapore, Singapore. ✉e-mail: daniel.leykam@gmail.com

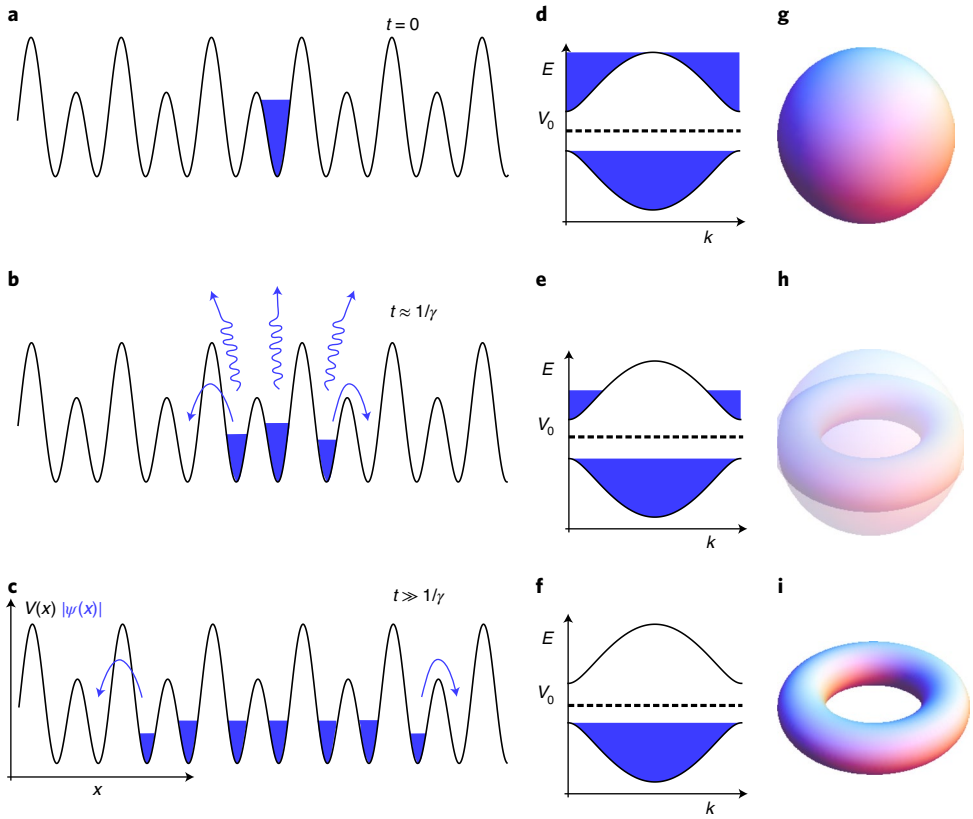

Fig. 1 | Schematic of the method to measure topological invariants using leaky lattices. a–c, Real-space dynamics, $\psi(x,t)$, of a spatially localized excitation (**a**), which radiates energy as it spreads through the lattice (**b**) until only the bound modes remain (**c**). **d–i**, Filling of the lattice's Bloch bands (denoted by the shaded blue regions) at various times. At $t=0$, all the bands are excited (**d**), corresponding to a topologically trivial field represented by a sphere (**g**). At intermediate times comparable to the lifetime of the leaky modes ($1/\gamma$), the bands with energies above the environment potential V_0 are partially filled (**e**), corresponding to a field with an ill-defined topology represented by an overlapping sphere and torus (**h**). When $t \gg 1/\gamma$, only the bands with $E < V_0$ remain populated (**f**) and their topology is imprinted on the (still spreading) field, represented by a torus (**i**).

approximation assumes a deep lattice, such that each site hosts a bound mode that does not radiate energy to its environment. On the other hand, in shallow (leaky) lattices, the number of bound modes may be less than the number of lattice sites, and the detuning of the site energies with respect to the energy of their environment (V_0) plays a critical role, determining the transition between the bound and radiative modes.

When there is a sharp boundary between the lattice and its environment and no backscattering of waves from the environment, one can introduce quasi-normal modes to describe the wave dynamics in shallow lattices[11–16]. Quasi-normal modes are calculated by eliminating the continuum of radiation modes to obtain an eigenvalue problem on a finite domain with outgoing-wave boundary conditions. Because the radiation rate depends on the modal energy, this eigenvalue problem is, in general, nonlinear. For simplicity, in the following, we assume that radiation occurs via independent one-dimensional channels described by dispersion relations of the form $E(k) = V_0 + k^2/(2m_{\mathrm{eff}})$. The resulting quadratic eigenvalue problem can be linearized as (see Supplementary Section 1 for details)[32]

$$\begin{pmatrix} \frac{1}{\sqrt{2m_{\mathrm{eff}}}}\hat{\Gamma} & \hat{H} - V_0\hat{1} \\ -\hat{1} & 0 \end{pmatrix} |\Phi\rangle = -\frac{\xi}{\sqrt{2m_{\mathrm{eff}}}}|\Phi\rangle, \qquad (3)$$

where $\xi = \sqrt{2m_{\mathrm{eff}}(V_0 - E - i\gamma)}$ is the field decay rate in the environment, $|\Phi\rangle = \left(\frac{\xi}{\sqrt{2m_{\mathrm{eff}}}}|\phi\rangle, |\phi\rangle\right)^T$ is an auxiliary vector from which the modal profile $|\phi\rangle$ can be obtained, and $\hat{\Gamma}$ describes the coupling of the individual sites to the environment. When $\hat{H}$ is Hermitian, the modes shown in equation (3) have purely real eigenvalues for $E < V_0$; they only acquire complex eigenvalues for $E > V_0$ (ref. [11]).

The transition between real and complex eigenvalues corresponds to a non-Hermitian degeneracy at which the incoming and radiating quasi-normal modes coalesce. Such energy-dependent losses provide a novel kind of non-Hermitian dynamics, in contrast to equation (2), where non-Hermitian perturbations generally give all the eigenvalues nonzero imaginary parts in the absence of any special symmetries (for example, parity–time symmetry[30]). In particular, waves propagating in a leaky lattice radiate energy from all the modes with energies $E > V_0$, while conserving the population of the modes with energies $E < V_0$.

As an example of this sharp transition between the bound and leaky modes, Fig. 2a shows the quasi-normal mode spectrum of a finite one-dimensional lattice, which we obtain by numerically solving equation (1) using outgoing-wave boundary conditions. As the environmental potential depth V_0 decreases, the array modes become leaky one by one, each exhibiting a sharp transition from real to complex eigenvalues. The leaky modes' loss is determined by both their energy and how strongly their spatial profile overlaps with the lattice boundary. We find a good qualitative agreement between the numerical solution and an $L=6$ site effective tight-binding model of the form $\hat{H} = J\sum_{m=1}^{L-1}(\hat{a}_m^\dagger \hat{a}_{m+1} + \hat{a}_{m+1}^\dagger \hat{a}_m)$ with the environmental coupling $\frac{1}{\sqrt{2m_{\mathrm{eff}}}}\hat{\Gamma} = \varepsilon(\hat{a}_1^\dagger \hat{a}_1 + \hat{a}_L^\dagger \hat{a}_L)$, as shown in Fig. 2b. Supplementary Section 2 provides a quantitative comparison for a two-site lattice.

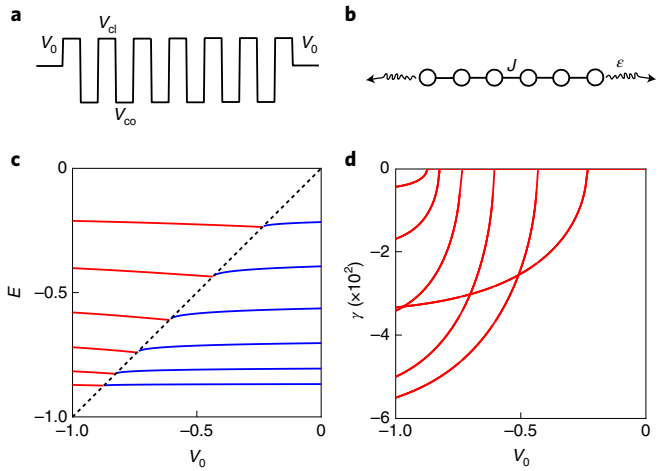

Fig. 2 | Quasi-normal mode spectrum of a one-dimensional lattice. **a**, Potential profile with V_{co} and V_{cl} being the alternating core and cladding potential levels, respectively. **b**, Corresponding tight-binding model, with intersite coupling J and environmental coupling ε. **c**, Modal energies E; purely real eigenvalues are plotted in blue, while leaky modes shown in red emerge when E crosses the environmental potential V_0 (black dashed line). **d**, Growth rates, γ, of the leaky modes.

Band projection using leaky lattices

It is particularly interesting to apply the above quasi-normal mode formalism to multiband lattices, where tuning V_0 into a bandgap allows one to filter out the higher band components of arbitrary initial states without requiring prior knowledge of the lattice's eigenmodes. This enables the measurement of the band projection operators $\hat{P} = \sum_{E(\phi) < V_0} |\phi\rangle\langle\phi|$, from which any observable of the filled bands can be obtained, including their topological invariants. This is our central result.

To obtain $\hat{P}$, one should prepare a set of incoherent normalized initial states $|\psi_j(0)\rangle$ indexed by j, whose evolution is described by the time-dependent (unnormalized) density matrix $\hat{\rho}(t) = \sum_j |\psi_j(t)\rangle\langle\psi_j(t)| = \mathrm{e}^{-i\hat{H}t}\hat{\rho}(0)\mathrm{e}^{i\hat{H}t}$. If the initial states form a complete basis for the lattice such that $\hat{\rho}(0) = \hat{1}$, then in the long time limit $t \gg 1/\gamma_0$, where γ_0 is the lifetime of the longest-lived leaky mode, $\hat{\rho}(t) \to \hat{P}$. This follows from the band projector being idempotent ($\hat{P}^2 = \hat{P}$) and commuting with $\hat{H}$ ($[\hat{H}, \hat{P}] = 0$). Thus, $\hat{P}$ can be obtained by measuring the elements of $\hat{\rho}(t)$ at large t.

The diagonal elements of $\hat{\rho}(t)$ correspond to the intensities or populations of the lattice sites m, summed over the different excitations, that is, $\rho_{mm} = \sum_j |\phi_{mj}(t)|^2$. The off-diagonal elements, $\rho_{mm'} = \sum_j \phi_{mj}\phi^*_{m'j}$, depend on the relative phase between pairs of sites (m, m'). Both can be readily measured in cold atom or photonic setups. In the former, one can use an optical lattice with laser-assisted tunnelling, suddenly switching off some of the intersite couplings at time t such that only pairs of neighbouring sites are coupled together and then observing the resulting double-well oscillations[33]. In photonics, the site phases can be extracted using a combination of near- and far-field intensity measurements[34] or via interference with a weak tilted reference beam[35].

In the special case of translation-invariant (or weakly disordered) lattices, the preparation and measurement of $\hat{\rho}$ simplifies considerably: in the momentum ($\mathbf{k}$) basis, $\hat{P}$ and $\hat{\rho}$ are block diagonal; at large t, the elements of $\hat{\rho}$ become independent of time (Methods and Supplementary Section 3). Thus, $\hat{\rho}$ can be obtained by summing over N initial states, where N is the number of energy bands. Each state should be localized to a single unit cell (thereby having a flat spectrum in $\mathbf{k}$ space); together, they should form a complete basis for the lattice's internal (sublattice or spin) degree of freedom. For example, in a waveguide lattice, one should excite, in turn, each sublattice of a single unit cell. This approach is similar, in spirit, to Brillouin zone spectroscopy[36]. In the following sections, we show how the lattice's topological invariants can be measured using $\hat{P}(\mathbf{k})$ obtained in this manner.

Zak phase in the SSH model

As the first example of measuring the topological invariants using leaky photonic lattices, we consider the SSH Hamiltonian $\hat{H} = \hat{H}_{\mathrm{SSH}}$, which exhibits two topological phases distinguished by the quantized Zak phase $\nu = 0$ or π (Methods). For simplicity, we assume that all the sites have the same environmental coupling $\hat{\Gamma}/\sqrt{2m_{\mathrm{eff}}} = \varepsilon \sum_{m=1}^{L} \left(\hat{a}_m^\dagger \hat{a}_m + \hat{b}_m^\dagger \hat{b}_m\right)$, corresponding to a waveguide array with dimerized couplings $J_1 \neq J_2$ and radiative losses occurring transverse to the lattice[35].

Figure 3a–c shows how the spectrum of the eigenvalue problem for the quasi-normal modes in equation (3) depends on the environmental potential depth V_0. When V_0 exceeds the largest eigenvalue of $\hat{H}$ ($V_0 > J_1 + J_2$), all the modes are bound and have real energies, such that the system is effectively Hermitian. As V_0 decreases, the Bloch modes start to become leaky, radiating their energy into the environment and acquiring finite lifetimes. When $|J_1 - J_2| < V_0 < J_1 + J_2$, the transition between the leaky and bound modes lies within the upper Bloch band, and thus, the number of bound modes is sensitive to the precise value of V_0, analogous to a metallic electronic phase. On the other hand, when V_0 lies in the bulk bandgap, namely, $|V_0| < |J_1 - J_2|$, the number of bound modes is independent of V_0, analogous to an electronic insulating phase.

To demonstrate that these different regimes exhibit different dynamical properties, we simulate the time evolution of single bulk waveguide excitations via projection onto the lattice's quasi-normal modes. Figure 3d shows the plots of the dynamics of the wavepacket norm for various V_0 values:

$$\mathcal{N}(t) = \sum_{m=1}^{L} (|\psi_{a,m}(t)|^2 + |\psi_{b,m}(t)|^2), \tag{4}$$

where the initial states are normalized such that $\mathcal{N}(0) = 1$. In the Hermitian regime, the norm remains conserved, while in the metallic regime, $\mathcal{N}$ decays to a limiting value sensitive to V_0. In the insulating regime, $\mathcal{N}(t) \to 1/2$ as the upper band radiates all its energy, enabling the measurement of the band projection operator $\hat{P}(k)$ using the density matrix $\hat{\rho}(k, t)$. We quantify the accuracy of this measurement using the momentum-averaged error as follows:

$$\overline{\Delta P}(t) = \frac{1}{L} \sum_k \left[\sum_{i,j=a,b} |\rho_{ij}(k, t) - P_{ij}(k)|^2 \right]^{1/2}. \tag{5}$$

Figure 3e shows that in the insulating regime, this error becomes small once the upper band has depopulated. Note that in this finite lattice, $\overline{\Delta P}(t)$ does not converge exactly to zero because after a sufficiently long time, the wavepacket reflects off the array edges, such that the momentum-space form of the projector $\hat{P}(k)$ (which assumes periodic boundary conditions) is no longer valid. We stress that in finite systems, the real-space form of $\hat{P}$ remains well defined, and one can still measure the quantized topological invariants[19–21].

Finally, Fig. 3f shows the Zak phase, ν, obtained using the field projection operator, that is, equations (13) and (16), in the presence of weak disorder in the coupling coefficients $\delta J \in [-W/2, W/2]$, where $W = 0.1J$. The Zak phase measured via $\hat{\rho}$ remains robust in the insulating regime, converging to its quantized value of 0 or π depending on whether the system is trivial or non-trivial; as the field

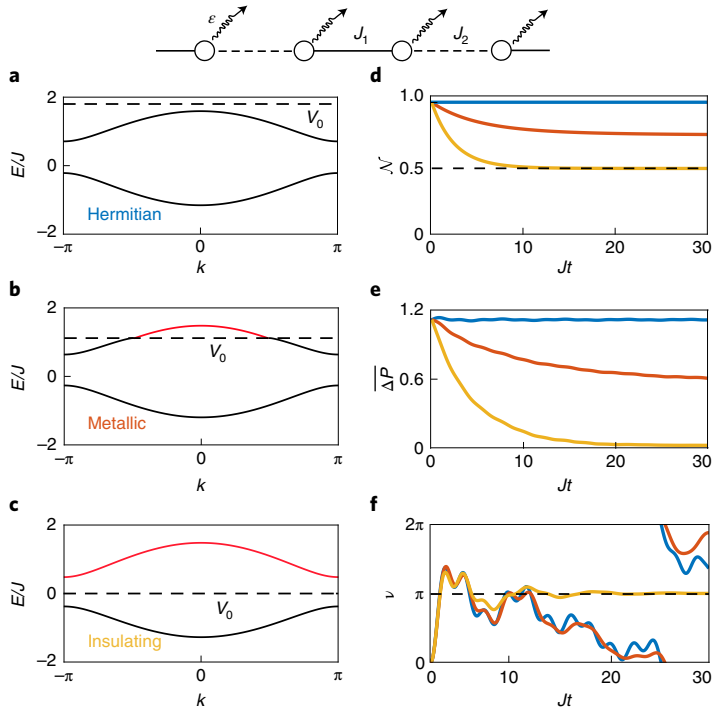

Fig. 3 | Leaky SSH lattice. a–c, Bloch wave spectra for environmental potentials V_0 (dashed line) in three regimes: 'Hermitian' ($V_0 = 1.8J$) (**a**), 'metallic' ($V_0 = 1.1J$) (**b**) and 'insulating' ($V_0 = 0$) (**c**). Red lines denote the leaky modes above V_0. **d–f**, Dynamics in the Hermitian (blue), metallic (brown) and insulating (gold) regimes. **d**, Total wavepacket norm $\mathcal{N}$, which is conserved in the Hermitian limit, decays to a V_0-dependent limiting value in the metallic regime and to 50% in the insulating regime. **e**, Mean error in the band projection operator estimated using the wavepacket projector, which approaches zero in the insulating regime. **f**, Zak phase measured using the extracted band projection operator, which converges to a quantized limiting value in the insulating regime, even in the presence of the coupling disorder. We use parameters $J_1 = J/2$, $J_2 = J$ and $\varepsilon = 0.2J$.

spreads through the lattice, it effectively averages over different local values of the disorder. As long as the disorder is weak enough (that is, a sufficiently long Anderson localization length) to achieve this averaging, the result will be a good approximation to ν. For stronger disorders, one can still accurately measure ν by averaging over multiple input positions[19]. In contrast, previous approaches to measure the Zak phase based on the mean wavepacket displacement[37–40] no longer work in disordered lattices, because the displacement is sensitive to the local disorder potential near the initially excited site.

Chern number in the Haldane model

The SSH model is a convenient test bed for exploring the measurement of bulk topological invariants, but is somewhat pathological because the value of the bulk invariant depends on the arbitrary choice of the unit cell boundary. We now show that leaky lattices can also be used to measure two-dimensional topological invariants (such as the Chern number), which remain quantized even in the absence of sublattice symmetries[21].

For our numerical demonstration, we use the Haldane model (schematic shown in Fig. 4a) and again assume that the environmental coupling is uniform for all the sites. The full details of the simulations can be found in Methods. Figure 4b shows the dynamics of the extracted Chern number C in the three different regimes (Hermitian, metallic and insulating). Here C only converges to the correct quantized value in the insulating regime; otherwise, the measured field profiles do not yield the band projection operator due to persistent interference between the two bands.

In Fig. 4c, we show the phase diagram of the full Haldane model extracted from $\hat{\rho}(\mathbf{k}, t)$ in the insulating regime. Deep in the gapped phases, the correct Chern numbers, namely, $C = 0, \pm 1$, are reproduced, while errors appear close to the phase boundaries. There are two main sources of error. (1) When the gap is small, modes near the upper band edge decay slowly and may have some residual population at the measurement time, spoiling the measurement of $\hat{P}$. (2) If the Berry curvature is strongly localized within the Brillouin zone, it may not be faithfully captured by the discretized Fourier space grid. For our choice of parameters, the latter dominates; thus, the error is reduced by increasing the lattice size. Figure 4d demonstrates that the extracted Chern number is robust against moderate on-site disorder described by $\hat{V} = \sum_m (V_{a,m}\hat{a}_m^\dagger \hat{a}_m + V_{b,m}\hat{b}_m^\dagger \hat{b}_m)$, where $V_{a,m}$ and $V_{b,m}$ are uniformly distributed in $[-W/2, W/2]$.

Slab waveguide implementation

To show that the measurement of the bulk topological invariants using leaky lattices is not limited to tight-binding models, we now consider the propagation of transverse electric polarized optical beams $\psi(x, z)$ in a one-dimensional slab waveguide array or photonic crystal governed by the Helmholtz equation:

$$\partial_z^2 \psi(x, z) = -\left[\partial_x^2 + k_0^2 n^2(x)\right]\psi(x, z), \tag{6}$$

where the refractive index profile $n(x)$ plays the role of the potential. For our simulations, we use a wavelength of $\lambda = 1.55\,\mu$m, waveguides of width $w = 0.5\,\mu$m with core index $n_{co} = 1.5$, separated by cladding with mean width $d = 0.33\,\mu$m and cladding index $n_{cl} = 1$. We stagger the cladding widths by $\delta = \pm 0.17\,\mu$m to create the $(L = 10)$-waveguide trivial and non-trivial SSH lattices, as shown in Fig. 5a,b; further, the environmental index $n_0 = 1.26$ is set to lie in its bulk bandgap. We stress that the precise values of n_{co} and n_{cl} are unimportant provided the index contrast between n_{co} and n_{cl} remains similar and n_0 lies in the bulk bandgap of the array. The latter can be achieved by embedding the array within an appropriately designed photonic crystal or

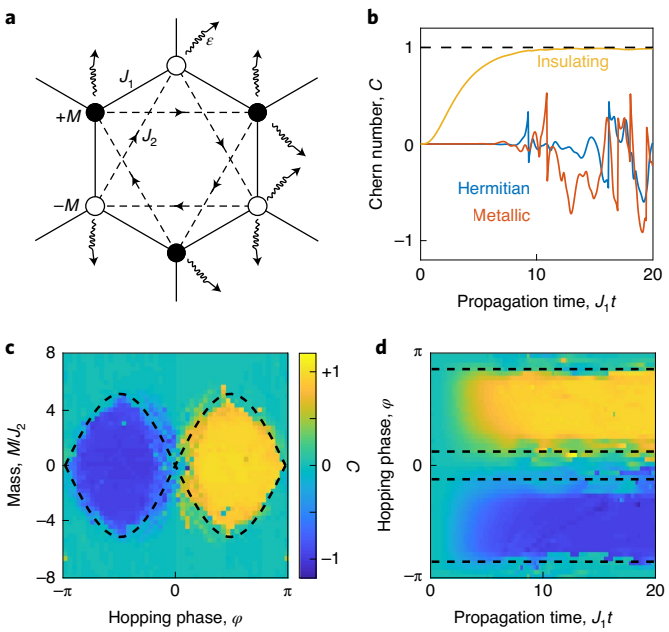

Fig. 4 | Measurement of Chern numbers using the leaky Haldane model. **a**, Model schematic. **b**, Dynamics of the extracted Chern number in the three different regimes (Hermitian, $V_0=4J_1$; metallic, $V_0=2J_2$; insulating, $V_0=0$) for $M=0$ and $\varphi=\pi/2$. **c**, Phase diagram extracted from the insulating lattice. **d**, Dynamics of the extracted Chern number in lattices with disorder $\in[-W/2, W/2]$ in the on-site potentials, $W=M=2J_2$. The black dashed lines in **c** and **d** indicate the exact phase boundaries of the Hermitian tight-binding Hamiltonian.

metamaterial environment[41]. For example, one could use a dielectric multilayer structure formed by alternating layers of silicon nitride and glass, with radiation leakage finely tuned by the metal gratings deposited on the edges of the stack[42].

We numerically solve equation (6) using a finite-element-method solver in COMSOL Multiphysics. To implement radiation losses, we impose perfectly matched layers at the transverse edges of the simulation domain. We include coupling disorder by introducing small z-independent variations in the waveguide separations (up to 5% of the minimum spacing). Figure 5a,b shows the evolution of an initially localized beam, which spreads throughout the array and radiates energy into the environment.

The imaginary part of the array modes' effective indices $\mathrm{Im}(n_{\mathrm{eff}})\gtrsim10^{-3}$ corresponds to the leaky modes decaying within a propagation distance of $z\lesssim400\,\mu$m, resulting in the convergence of the total power in the array to a limiting value, as shown in Fig. 5c. Since the environmental coupling occurs only via the ends of the array, the presence of edge states in the non-trivial phase increases the lifetime of its bulk modes, which explains the slower convergence observed. Nevertheless, both trivial and non-trivial arrays converge to the same final power. Note that due to the strong overlap between the different waveguide modes, the power does not converge to the ideal value of 50% observed in the tight-binding model.

Before turning to the calculation of the Zak phase using the field projection operator, we first discuss the behaviour of the mean wavepacket displacement Δx:

$$\Delta x(z)=x(z)-x(0),\quad x(z)=\frac{1}{2\mathcal{N}(z)}\sum_{m=1}^{L}m|\psi_m(z)|^2,\qquad(7)$$

where $x(z)$ is the centre of mass of the beam (normalized to the array period) and ψ_m is the field amplitude in the mth waveguide. Δx was previously used to extract the Zak phase by either using the loss localized on one of the sublattices[37,38], measuring its z average[39], or performing energy-resolved measurements[40]. Due to the coupling disorder, the wavepacket displacement (shown in Fig. 5d) does not oscillate about or converge to any quantized value, and thus, the field projection operator is required to determine the Zak phase.

Figure 5e shows a rapid convergence to the correct Zak phase in the trivial lattice, even without summing the field projector over excitations of the two sublattices. On the other hand, the non-trivial array (shown in Fig. 5f) exhibits slower convergence, which can be attributed to its lower losses and our small system size. These numerical results establish that our theory remains valid for small systems, and it does not require any tight-binding approximation.

Discussion

We have shown how non-interacting waves propagating in shallow lattices can be described by a novel class of tight-binding

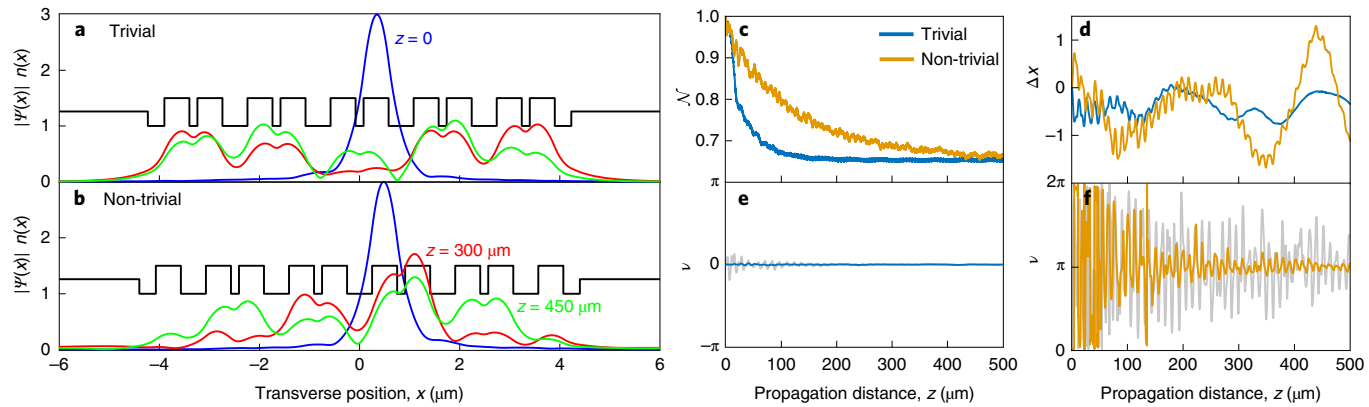

Fig. 5 | Array of ten slab waveguides for implementing the SSH model. **a**,**b**, Refractive index profile (black) and electric field profile $|\psi|$ at propagation distances of $z=0$ (blue), $z=300\,\mu$m (red) and $z=450\,\mu$m (green) in the trivial ($\delta=-0.17\,\mu$m) (**a**) and non-trivial ($\delta=0.17\,\mu$m) (**b**) lattices. **c**,**d**, Dynamics of the total norm $\mathcal{N}$ (**c**) and mean wavepacket displacement Δx (**d**) in the trivial (blue) and non-trivial (gold) lattices. **e**,**f**, Zak phase ν obtained from the field projection operator summed over the excitations of the fifth and sixth waveguides in the trivial (**e**) and non-trivial (**f**) lattices. For comparison, the grey curves show the Zak phase estimated from a single waveguide excitation.

models with energy-dependent losses. Different propagation regimes emerge depending on the energy detuning between the lattice and its environment: 'Hermitian' (lossless), 'metallic' (sensitive to the detuning) and 'insulating' (insensitive to the detuning). At long propagation times, the field profile in the insulating regime allows the measurement of the band projection operator and quantized topological invariants. Leaky lattices are more flexible than existing approaches for measuring topological invariants using propagation dynamics, which either exploit the known symmetries of the Hamiltonian[43] or require time-consuming band tomography using a spatially broad initial wavepacket tailored to excite a single band[9]. Moreover, our approach remains valid for disordered systems.

We have validated our scheme using the SSH and Haldane models and numerical simulations of light propagation in a slab waveguide array. In Supplementary Section 4, we show how our models can also be implemented using existing platforms for topological lattices such as deep waveguide arrays fabricated using direct laser writing[38,39,44] (Extended Data Fig. 1) and silicon lithography[45] (Extended Data Fig. 2). The former uses auxiliary waveguides as an environment, similar to ref. [26], while the environmental potential depth in the latter can be fine-tuned by adjusting the height of deposited silicon.

For simplicity, we focused on the measurement of topological invariants in Fourier space, which assumes a periodic lattice. However, according to refs. [19–21], one can also use real-space topological markers to obtain the bulk topological invariants by measuring the correlation functions of the field. An interesting future direction is to use leaky photonic lattices to study the real-space dynamics of correlation functions such as the Chern marker[46].

In the insulating regime, when the detuning of the leaky bands from the cutoff V_0 is much larger than the environmental coupling strength, the modal losses γ become approximately proportional to their energy detuning, namely, $\gamma=(V_0-E)\alpha$, where α is some constant factor. Consequently, at finite times (before the leaky bands have completely depopulated), the modal populations $\propto e^{-(V_0-E)/T}$ resemble Boltzmann factors with effective temperature $T=1/(\alpha t)$. Thus, leaky lattices may also provide a platform to emulate topological systems at a finite temperature[47].

Finally, leaky lattices are also a highly promising platform for studying related topics such as non-Hermitian systems and non-Hermitian topological phases[22–31]. Our models based on the non-interacting Schrödinger equation are applicable to various bosonic wave systems including light propagation in waveguide arrays and photonic crystals, as well as acoustics and Bose–Einstein condensates, where the phenomena we have discussed may be further enriched by effects such as spin–orbit coupling and interparticle interactions.

Online content

Any methods, additional references, Nature Research reporting summaries, source data, extended data, supplementary information, acknowledgements, peer review information; details of author contributions and competing interests; and statements of data and code availability are available at https://doi.org/10.1038/s41567-020-01144-5.

Received: 6 May 2020; Accepted: 7 December 2020;
Published online: 11 February 2021

References

1. Hasan, M. Z. & Kane, C. L. Colloquium: topological insulators. *Rev. Mod. Phys.* **82**, 3045 (2010).
2. Ozawa, T. et al. Topological photonics. *Rev. Mod. Phys.* **91**, 015006 (2019).
3. Goldman, N., Budich, J. C. & Zoller, P. Topological quantum matter with ultracold gases in optical lattices. *Nat. Phys.* **12**, 639–645 (2016).
4. Ma, G., Xiao, M. & Chan, C. T. Topological phases in acoustic and mechanical systems. *Nat. Rev. Phys.* **1**, 281–294 (2019).
5. Hu, W. et al. Measurement of a topological edge invariant in a microwave network. *Phys. Rev. X* **5**, 011012 (2015).
6. Mittal, S., Ganeshan, S., Fan, J., Vaezi, A. & Hafezi, M. Measurement of topological invariants in a 2D photonic system. *Nat. Photon.* **10**, 180–183 (2016).
7. Bardyn, C.-E., Huber, S. D. & Zilberberg, O. Measuring topological invariants in small photonic lattices. *New J. Phys.* **16**, 123013 (2014).
8. Aidelsburger, M. et al. Measuring the Chern number of Hofstadter bands with ultracold bosonic atoms. *Nat. Phys.* **11**, 162–166 (2015).
9. Wimmer, M., Price, H. M., Carusotto, I. & Peschel, U. Experimental measurement of the Berry curvature from anomalous transport. *Nat. Phys.* **13**, 545–550 (2017).
10. Tarnowski, M. et al. Measuring topology from dynamics by obtaining the Chern number from a linking number. *Nat. Commun.* **10**, 1728 (2019).
11. Ching, E. S. C. et al. Quasinormal-mode expansion for waves in open systems. *Rev. Mod. Phys.* **70**, 1545–1554 (1998).
12. Hu, J. & Menyuk, C. R. Understanding leaky modes: slab waveguide revisited. *Adv. Opt. Photon.* **1**, 58–106 (2009).
13. Monticone, F. & Alù, A. Leaky-wave theory, techniques, and applications: from microwaves to visible frequencies. *Proc. IEEE* **103**, 793–821 (2015).
14. Stowell, D. & Tausch, J. Variational formulation for guided and leaky modes in multilayer dielectric waveguides. *Commun. Comput. Phys.* **7**, 564–579 (2010).
15. Powell, D. A. Interference between the modes of an all-dielectric meta-atom. *Phys. Rev. Appl.* **7**, 034006 (2017).
16. Pick, A. & Moiseyev, N. Polarization dependence of the propagation constant of leaky guided modes. *Phys. Rev. A* **97**, 043854 (2018).
17. Lalanne, P., Yan, W., Vynck, K., Sauvan, C. & Hugonin, J.-P. Light interaction with photonic and plasmonic resonances. *Laser Photon. Rev.* **12**, 1700113 (2018).
18. Fukui, T., Hatsugai, Y. & Suzuki, H. Chern numbers in discretized Brillouin zone: efficient method of computing (spin) Hall conductances. *J. Phys. Soc. Jpn* **74**, 1674–1677 (2005).
19. Bianco, R. & Resta, R. Mapping topological order in coordinate space. *Phys. Rev. B* **84**, 241106(R) (2011).
20. Ringel, Z. & Kraus, Y. E. Determining topological order from local ground-state correlation function. *Phys. Rev. B* **83**, 245115 (2011).
21. Chiu, C.-K., Teo, J. C. Y., Schnyder, A. P. & Ryu, S. Classification of topological quantum matter with symmetries. *Rev. Mod. Phys.* **88**, 035005 (2016).
22. Golshani, M. et al. Impact of loss on the wave dynamics in photonic waveguide lattices. *Phys. Rev. Lett.* **113**, 123903 (2014).
23. Longhi, S., Gatti, D. & Della Valle, G. Non-Hermitian transparency and one-way transport in low-dimensional lattices by an imaginary gauge field. *Phys. Rev. B* **92**, 094204 (2015).
24. Longhi, S. Non-Hermitian tight-binding network engineering. *Phys. Rev. A* **93**, 022102 (2016).
25. Leykam, D., Flach, S. & Chong, Y. D. Flat bands in lattices with non-Hermitian coupling. *Phys. Rev. B* **96**, 064305 (2017).
26. Mukherjee, S. et al. Dissipatively coupled waveguide networks for coherent diffusive photonics. *Nat. Commun.* **8**, 1909 (2017).
27. Esaki, K., Sato, M., Hasebe, K. & Kohmoto, M. Edge states and topological phases in non-Hermitian systems. *Phys. Rev. B* **84**, 205128 (2011).
28. Gong, Z. et al. Topological phases of non-Hermitian systems. *Phys. Rev. X* **8**, 031079 (2018).
29. Gorlach, M. A. et al. Far-field probing of leaky topological states in all-dielectric metasurfaces. *Nat. Commun.* **9**, 909 (2018).
30. El-Ganainy, R. et al. Non-Hermitian physics and PT symmetry. *Nat. Phys.* **14**, 11–19 (2018).
31. Yoshida, T. & Hatsugai, Y. Exceptional rings protected by emergent symmetry for mechanical systems. *Phys. Rev. B* **100**, 054109 (2019).
32. Tisseur, F. & Meerbergen, K. The quadratic eigenvalue problem. *SIAM Rev.* **43**, 235–286 (2001).
33. Atala, M. et al. Observation of chiral currents with ultracold atoms in bosonic ladders. *Nat. Phys.* **10**, 588–593 (2014).
34. Gerchberg, R. W. & Saxton, W. O. A practical algorithm for the determination of the phase from image and diffraction plane pictures. *Optik* **35**, 237–246 (1972).
35. Malkova, N., Hromada, I., Wang, X., Bryant, G. & Chen, Z. Observation of optical Shockley-like surface states in photonic superlattices. *Opt. Lett.* **34**, 1633–1635 (2009).
36. Bartal, G. et al. Brillouin zone spectroscopy of nonlinear photonic lattices. *Phys. Rev. Lett.* **94**, 163902 (2005).
37. Rudner, M. S. & Levitov, L. S. Topological transition in a non-Hermitian quantum walk. *Phys. Rev. Lett.* **102**, 065703 (2009).
38. Zeuner, J. M. et al. Observation of a topological transition in the bulk of a non-Hermitian system. *Phys. Rev. Lett.* **115**, 040402 (2015).

39. Wang, Y. et al. Direct observation of topology from single-photon dynamics. *Phys. Rev. Lett.* **112**, 193903 (2019).
40. St-Jean, P. et al. Measuring topological invariants in polaritonic graphene. Preprint at https://arxiv.org/abs/2002.09528 (2020).
41. Cerjan, A., Hsu, C. W. & Rechtsman, M. C. Bound states in the continuum through environmental design. *Phys. Rev. Lett.* **123**, 023902 (2019).
42. Wang, Q. et al. Measurement of the Zak phase of photonic bands through the interface states of a metasurface/photonic crystal. *Phys. Rev. B* **93**, 041415(R) (2016).
43. Longhi, S. Probing topological phases in waveguide superlattices. *Opt. Lett.* **44**, 2530–2533 (2019).
44. Noh, J., Huang, S., Chen, K. P. & Rechtsman, M. C. Observation of photonic topological valley Hall edge states. *Phys. Rev. Lett.* **120**, 063902 (2018).
45. Blanco-Redondo, A. et al. Topological optical waveguiding in silicon and the transition between topological and trivial defect states. *Phys. Rev. Lett.* **116**, 163901 (2016).
46. Caio, M. D., Möller, G., Cooper, N. R. & Bhaseen, M. J. Topological marker currents in Chern insulators. *Nat. Phys.* **15**, 257–261 (2019).
47. Viyuela, O., Rivas, A. & Martin-Delgado, M. A. Uhlmann phase as a topological measure for one-dimensional fermion systems. *Phys. Rev. Lett.* **112**, 130401 (2014).

Methods

Band projection in periodic lattices. Consider the evolution of an arbitrary excitation $\left|\psi_j(\mathbf{k},t)\right\rangle$ of a translation-invariant leaky lattice with N bands, described by a Bloch Hamiltonian $\hat{H}(\mathbf{k})$ with Bloch function eigenmodes $|u_n(\mathbf{k})\rangle$, where $\mathbf{k}$ is the Bloch momentum, $n=1,\ldots,N$ is the band index, the bra–ket notation encodes the internal (sublattice or spin-like) degrees of freedom within each unit cell and j indexes the different initial states. The field's Fourier transform $\left|\psi_j(\mathbf{k},t)\right\rangle$ can be expressed as a superposition of modes from different bands:

$$\left|\psi_j(\mathbf{k},t)\right\rangle = \sum_{n=1}^{N} c_{jn}(\mathbf{k})\mathrm{e}^{-i[E_n(\mathbf{k})+i\gamma_n(\mathbf{k})]t}|u_n(\mathbf{k})\rangle, \tag{8}$$

where $c_{jn}(\mathbf{k}) = \left\langle u_n(\mathbf{k})|\psi_j(\mathbf{k},0)\right\rangle$ are the Bloch function weights determined by the initial field profile.

The band projection operator $\hat{P}(\mathbf{k})$ can be obtained by introducing the unnormalized density matrix

$$\hat{\rho}(\mathbf{k},t) = \sum_j \left|\psi_j(\mathbf{k},t)\right\rangle\left\langle\psi_j(\mathbf{k},t)\right|. \tag{9}$$

Expanding $\hat{\rho}(\mathbf{k},t)$ using equation (8) (and dropping the $\mathbf{k}$ arguments for brevity) leads to

$$\hat{\rho}(t) = \sum_j \sum_{n,n'=1}^{N} c_{jn}c_{jn'}^{*}\mathrm{e}^{i(E_{n'}-E_n)t+(\gamma_{n'}+\gamma_n)t}|u_n\rangle\langle u_{n'}|. \tag{10}$$

Leaky modes with energies $E_n > V_0$ above the cutoff will have $\gamma_n < 0$, such that their weights become exponentially small at large t. Thus, the summation over all the bands can be replaced with summation over bands below the cutoff, which have purely real eigenvalues, namely

$$\hat{\rho}(t) \to \sum_j \sum_{E_{n,n'}<V_0} c_{jn}c_{jn'}^{*}\mathrm{e}^{i(E_{n'}-E_n)t}|u_n\rangle\langle u_{n'}|. \tag{11}$$

The only remaining time-dependent terms are interband terms with $n' \neq n$. The interband terms can be eliminated by measuring $\hat{\rho}(t)$ as either a time average or in real space. In the latter case, interband terms decay at least as fast as $\propto \sqrt{1/t}$ (Supplementary Information). Thus, after sufficiently long t, the only terms contributing substantially to the field projector are diagonal in the band index:

$$\hat{\rho}(t\to\infty) = \sum_{E_n<V_0}\left(\sum_j |c_{jn}(\mathbf{k})|^2\right)|u_n\rangle\langle u_n|. \tag{12}$$

Finally, we assume that the set of initial states forms a complete basis spanning the local internal (sublattice or spin) degrees of freedom such that $\sum_j |c_{jn}(\mathbf{k})|^2 = 1$. Then equation (12) simplifies to

$$\hat{\rho}(t\to\infty) = \sum_{E_n<V_0} |u_n(\mathbf{k})\rangle\langle u_n(\mathbf{k})| \equiv \hat{P}(\mathbf{k}), \tag{13}$$

Thus, at large t, the field density matrix converges to the band projection operator $\hat{P}(\mathbf{k})$.

SSH model. The tight-binding Hamiltonian of the SSH model is[35]

$$\hat{H} = \sum_{m=1}^{L}\left[J_1\hat{a}_m^{\dagger}\hat{b}_m + J_2\hat{a}_{m+1}^{\dagger}\hat{b}_m\right] + \text{h.c.} \tag{14}$$

where $\hat{a}_m^{\dagger}$ ($\hat{b}_m^{\dagger}$) creates a particle on the a (b) sublattice in the unit cell m; J_1 and J_2 are intra- and intercell hopping strengths, respectively; and the lattice consists of L unit cells. The corresponding Bloch Hamiltonian $\hat{H}(k)$ has a quantized Zak phase[48]

$$\nu = i\int_{-\pi}^{\pi} \mathrm{d}k\langle u(k)|\partial_k u(k)\rangle, \tag{15}$$

where $|u(k)\rangle$ is the Bloch function of the lower band. When $J_2 > J_1$, the system is in the topological phase with $\nu=\pi$, hosting zero-energy edge states. When $J_1 > J_2$, the system is in the trivial phase, namely, $\nu=0$. In finite lattices, the Zak phase can be recast into the discretized form[49]

$$\nu = \mathrm{Im}\ln\left(\mathrm{Tr}\left[\prod_{k_m}\hat{P}(k_m)\right]\right), \tag{16}$$

where $k_m = 2\pi m/L$ is the discretized momentum space.

For the demonstration shown in Fig. 3, we used a large ($L=64$) lattice, both to illustrate the convergence of our method to the exact quantized Zak phase and to ensure negligible edge effects for simplicity. Due to the chiral symmetry, a single-site input uniformly excites both bands, which conveniently enables the measurement of the band projector $\hat{P}(k)$ without having to construct $\hat{\rho}$ by summing multiple single-site excitations.

While our method can still be applied to small arrays, there are two additional sources of error that may reduce the accuracy of equation (13): (1) overlap of the initial excitation with the edge states, if they exist; (2) reflections off the edge, which can redistribute energy between different k values, spoiling the completeness relation. For the parameters used in Fig. 3, we have observed convergence to the correct Zak phase for modest system sizes of $L > 6$ unit cells.

Haldane model. The Haldane model is given by the tight-binding Hamiltonian[50]

$$\begin{aligned}\hat{H} = M\sum_m(\hat{a}_m^{\dagger}\hat{a}_m - \hat{b}_m^{\dagger}\hat{b}_m) + J_1\sum_{<m,m'>}(\hat{a}_m^{\dagger}\hat{b}_{m'} + \hat{b}_m^{\dagger}\hat{a}_{m'}) \\ +J_2\sum_{\ll m,m'\gg}(\hat{a}_m^{\dagger}\hat{a}_{m'}\mathrm{e}^{i\varphi_{mm'}} + \hat{b}_m^{\dagger}\hat{b}_{m'}\mathrm{e}^{-i\varphi_{mm'}}),\end{aligned} \tag{17}$$

where M is the detuning between the a and b sublattices; J_1 and J_2 are the nearest and next-nearest-neighbour hopping strengths, respectively; and flux sign $\varphi_{mm'} = \pm\varphi$ alternates between the adjacent next-nearest neighbours. The Chern number can be expressed in terms of the band projection operator $\hat{P}(\mathbf{k})$ as[21]

$$C = \frac{1}{2\pi i}\int_{\mathrm{BZ}} \mathrm{Tr}\left[\hat{P}(\mathbf{k})[\partial_{k_x}\hat{P}(\mathbf{k}), \partial_{k_y}\hat{P}(\mathbf{k})]\right]\mathrm{d}\mathbf{k}. \tag{18}$$

This formula for the Chern number involves the commutator of $\mathbf{k}$-space derivatives of the projection operators, which may be difficult to measure in practise. Luckily, equation (18) can be efficiently discretized by replacing the $\mathbf{k}$-space derivatives with products over plaquettes[18]. In the case of the two-band Haldane model, equation (18) can be discretized to

$$C = \frac{1}{2\pi i}\sum_{k_x,k_y}\ln\left(\mathrm{Tr}[\hat{P}_{k_x,k_y}\hat{P}_{k_x+1,k_y}\hat{P}_{k_x+1,k_y+1}\hat{P}_{k_x,k_y+1}]\right), \tag{19}$$

where $\hat{P}_{k_x,k_y}$ is the band projection operator defined on a discrete $\mathbf{k}$-space grid. Even relatively coarse grids (lattice width, ~10 unit cells) are usually sufficient to accurately measure C (ref. [18]).

For the numerical simulations shown in Fig. 4, we use a finite lattice with a width of 14 unit cells along each principal axis, with the nearest neighbour coupling $J_1=1$, next-nearest-neighbour coupling $J_2=0.2J_1$ and environmental coupling $\varepsilon=0.2J_1$. Single-site excitations of the a and b sublattices at the centre of the lattice are evolved up to a maximum time $J_1t=20$ by projecting onto the quasi-normal modes. Using the Fourier transforms of the final field profiles and equation (13), we obtain $\hat{P}$; then the Chern number can be computed using equation (19).

Data availability

Source data are provided with this paper. All other data that support the plots within this paper and other findings of this study are available from the corresponding author upon reasonable request.

Code availability

The code used to perform the numerical simulations within this paper is available from the corresponding author upon reasonable request.

References

48. Atala, M. et al. Direct measurement of the Zak phase in topological Bloch bands. *Nat. Phys.* **9**, 795–800 (2013).
49. Vanderbilt, D. *Berry Phases in Electronic Structure Theory* (Cambridge Univ. Press, 2018).
50. Haldane, F. D. M. Model for a quantum Hall effect without Landau levels: condensed-matter realization of the 'parity anomaly'. *Phys. Rev. Lett.* **61**, 2015–2018 (1988).

Acknowledgements

We thank A. Cerjan, Z. Chen, Y. Chong and M. Rechstman for illuminating discussions. D.L. was supported by the Institute for Basic Science (IBS-R024-Y1 and IBS-R024-D1). D.A.S. acknowledges funding from the Australian Research Council's Early Career Researcher Award (DE190100430) and the Russian Science Foundation (Grant No. 20-72-00148).

Author contributions

D.L. and D.A.S. both performed the research and wrote the manuscript.

Competing interests

The authors declare no competing interests.

Additional information

Extended data is available for this paper at https://doi.org/10.1038/s41567-020-01144-5.

Supplementary information is available for this paper at https://doi.org/10.1038/s41567-020-01144-5.

Correspondence and requests for materials should be addressed to D.L.

Peer review information *Nature Physics* thanks the anonymous reviewers for their contribution to the peer review of this work.

Reprints and permissions information is available at www.nature.com/reprints.

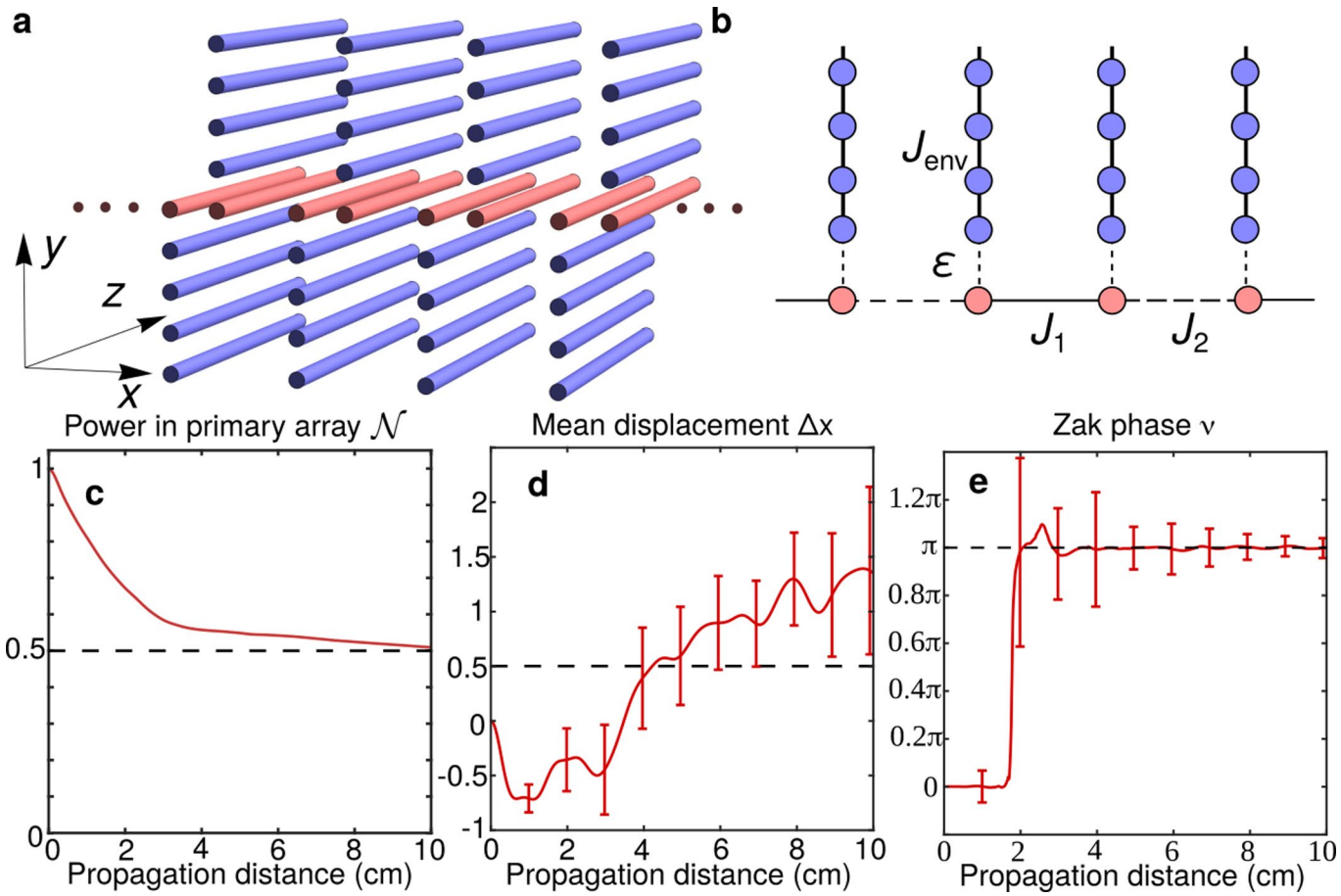

Extended Data Fig. 1 | Leaky photonic lattice design for laser-written waveguides. (a) Schematic of a leaky photonic lattice formed by an array of 18 primary waveguides (red) weakly coupled to auxiliary arrays forming the environment. The alternating position of the environment arrays above and below the primary array can be used to minimise unwanted direct coupling between the auxiliary arrays. (b) Corresponding tight binding model. (c,d,e) Dynamics of observables in the primary array: (c) the total norm $\mathcal{N} = \sum_m |\psi_m|^2$, (d) the mean displacement $\Delta x = \sum_m (m - x(0))|\psi_m|^2/\mathcal{N}$, and (e) the Zak phase ν. Error bars in (d,e) indicate one standard deviation obtained using an ensemble of 100 disorder realizations.

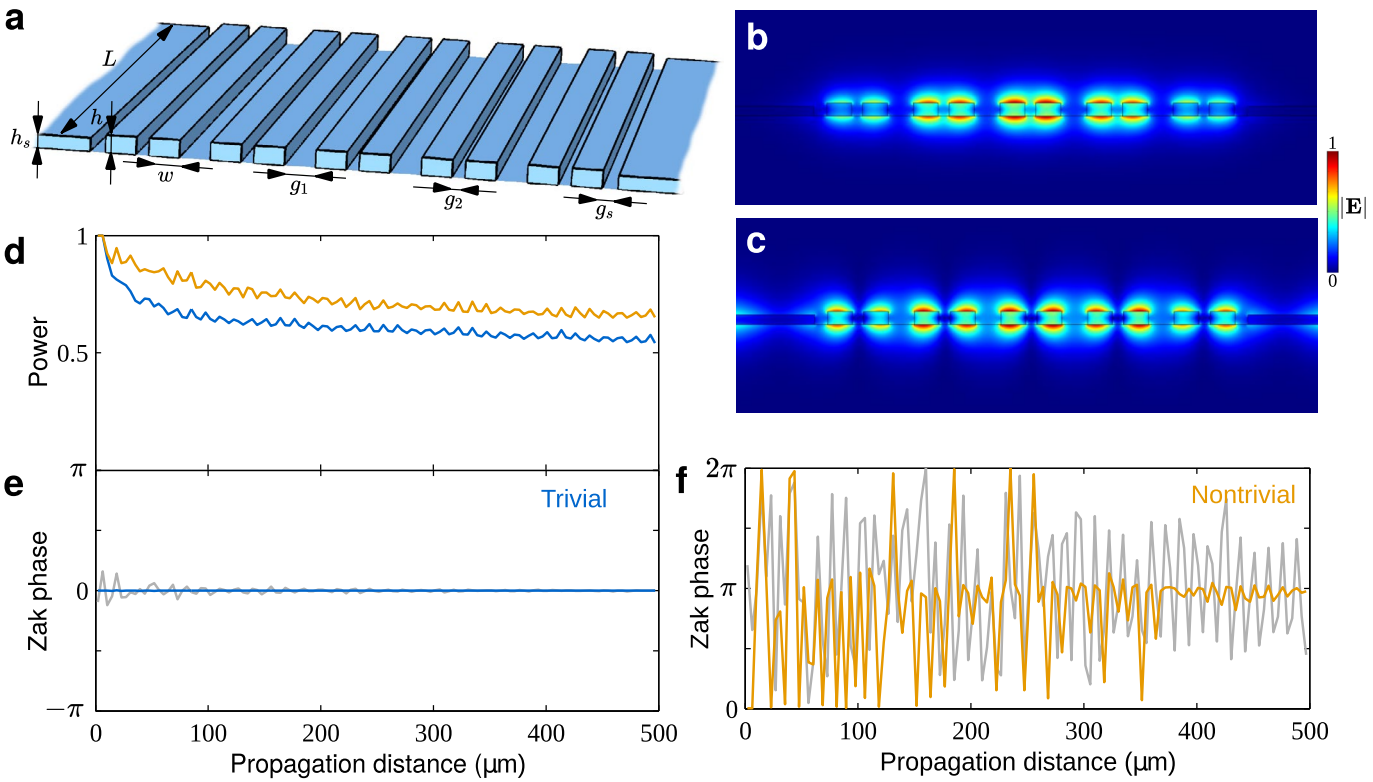

Extended Data Fig. 2 | Leaky photonic lattice design for silicon photonics. (a) Schematic of a dimerized array of 10 silicon waveguides with labelled dimensions. Trivial and nontrivial arrangements differ by the intersite gaps ordering: $g_1 > g_2$ (trivial), $g_1 < g_2$ (nontrivial). (b,c) Field profiles of eigenmodes from the upper (b, $n_{\text{eff}} = 1.8154$) and lower bands (c, $n_{\text{eff}} = 1.6735 - 0.0014i$) in the trivial array. (d) Power and (e,f) Zak phase obtained from the field projection operator summed over excitations of the 5th and 6th waveguides in the trivial (e, blue curves) and nontrivial (f, gold curves) arrays. For comparison, grey curves in (e,f) show the Zak phase estimated from the single 5th waveguide excitation.